Fuel 299 (2021) 120861

Contents lists available at ScienceDirect

Fuel

journal homepage: www.elsevier.com/locate/fuel

Full Length Article

# An experimental and one-dimensional modeling analysis of turbulent gas ejection in pre-chamber engines

J.M. García-Oliver [a,*], Y. Niki [b], R. Rajasegar [c], R. Novella [a], J. Gomez-Soriano [a], P.J. Martínez-Hernándiz [a], Z. Li [c], M.P.B. Musculus [c]

[a] CMT – Motores Térmicos, Universitat Politècnica de València, Camino de Vera, 46022 Valencia, Spain
[b] National Institute of Maritime, Port and Aviation Technology, Tokyo 181-0004, Japan
[c] Sandia National Laboratories, Livermore, CA, United States

ARTICLE INFO

*Keywords:*
Pre-chamber spark ignition
1-D gas jet model
cycle-to-cycle variability
infrared imaging
high-speed visualization

ABSTRACT

Experimental results from a study on the evolution of gas jets ejected through the orifices of a pre-chamber in a heavy-duty optical engine are presented. The work examines conditions without fuel inside the main-chamber, which helps to describe the dynamics of the ejected gas jets without the interference of subsequent combustion in the main-chamber. Experimental diagnostics consist of high-speed visible intensified imaging and low-speed infrared imaging. Additionally a one-dimensional gas jet model is used to characterize the spatial distribution of the ejected flow, including parameters such as tip penetration, which are then validated based on experimental results. Different stages in the ejection of pre-chamber jets are identified, with chemical activity restricted to a maximum distance of 5 to 10 orifice diameters downstream of the orifice as indicated by the recorded visible radiation. Sensitivity of cycle-to-cycle variations in pre-chamber jet development to the air-to-fuel ratio in the pre-chamber observed in the experiments is in most part attributed to the variations in the timing of combustion initiation in the pre-chamber. The influence of the ejection flow on the penetration of the gas jet on a cycle-to-cycle basis is presented using the one-dimensional model. The one-dimensional model also indicates that the local flow exhibits highest sensitivity to operating conditions during the start of ejection until the timing when maximum flow is attained. Differences that exist during the decreasing mass-flow ejection time-period tend to smear out in part due to the transient slowdown of the ejection process.

## 1. Introduction, motivation and objectives

In the search for higher thermal efficiency and lower fuel consumption in internal combustion engines, pre-chamber spark-ignition system is leading a new chapter in the improvement of spark-ignition engines' performance. The considerable increase in scientific publications related to this technology over the past few years demonstrates the appreciable growth in both scientific and commercial interests in pre-chamber spark-ignition systems. Many researchers have documented the main advantages of pre-chamber spark-ignition systems for use in high-power stationary power plants [1,2] and in transport applications [3–6] through several engine experiments. Under suitable operating conditions, pre-chamber spark-ignition guarantees extremely low cycle-to-cycle variation (CCV) and an accelerated combustion process [7], which minimizes knocking due to end-gas auto-ignition compared to conventional spark-ignition systems [8–11], and thus allows for an increase in the compression ratio that can further improve engine thermal efficiency [12]. In addition, its active version, with a dedicated fuel injector inside the pre-chamber, allows for an increase in the dilution limit to extremely lean mixtures ($\lambda \sim 2.5$), while reducing nitrogen oxides ($NO_x$) emissions to near zero levels [7,13].

Despite the general benefits of this ignition system being well established, the fundamental aspects of turbulent jet-based ignition are not fully understood, which hinders a complete concept optimization that in turn limits its market penetration [14]. For example, currently, there is no consensus on the combustion regimes that are encountered during the ejection of the gases from the pre-chamber at engine-relevant conditions involving ultra-lean mixtures.

To shed some light on this aspect, several researchers have utilized different visualization techniques applied to simplified devices such as divided constant-volume chambers and rapid compression machines (RCM). In a pioneering work [15] the visualization of pre-chamber

* Corresponding author.
*E-mail address:* jgarciao@mot.upv.es (J.M. García-Oliver).

https://doi.org/10.1016/j.fuel.2021.120861
Received 8 February 2021; Received in revised form 9 April 2021; Accepted 11 April 2021
Available online 3 May 2021

ignition process in a divided chamber bomb through high-speed schlieren imaging and OH* radiation was performed. Different ignition patterns were identified when modifying the nozzle diameter and the equivalence ratio in the main chamber. More recently, several experiments in a similar device using simultaneous high-speed schlieren [16] and OH* chemiluminescence imaging [17] were carried out to describe the jet penetration and ignition process. A relationship between the Damköhler number and the combustion regime in the main-chamber was established using semi-empirical correlations.

The temporal evolution of the ejected pre-chamber jets was related to the ignition kernel development within the pre-chamber in [18,19] using experimental visualizations and numerical simulation in a simplified pre-chamber apparatus at ambient pressure. The measurements showed the influence of the jet dynamic structure and mixture composition on the main-chamber ignition process. In particular, the authors emphasized on the importance of jet penetration length, jet duration, and reaction zone presence in the performance of this system.

The lack of fundamental analyses of the characteristics of premixed turbulent jets under engine-relevant conditions motivated other research works based on RCM optical measurements. In [20,21], the influence of nozzle diameter and equivalence ratio on jet morphology and ignition location in a radially mounted single hole pre-chamber was studied. Similarly, pre-chamber spark-ignition systems were compared in [22] with conventional systems using both high-speed OH* imaging and integrated UV emissions using a photomultiplier in an axially assembled four-nozzle pre-chamber that allowed for visualization of interaction between the reacting jets.

Despite some attempts involving studies based on real engine architecture to characterize the impact of the pre-chamber spark-ignition systems on the engine cycle-to-cycle variability, the root causes of this phenomenon have not been analyzed in detail due to facility limitations [23]. The complexity of applying visualization techniques in internal combustion engines due to the limited optical access increases significantly when considering a small dead volume (pre-chamber) connected by small orifices. Indeed, in small engines, it is practically impossible even to include a pressure transducer inside the pre-chamber. In this sense, there is an important dearth of knowledge related to the fundamentals of cycle-to-cycle variability in pre-chamber spark-ignited engines. Only the work in [24] delves into one of the possible root causes of CCV. They studied the asymmetries in the jet dynamics and structure of the pre-chamber jets (jet-to-jet variation) using numerical methods. Jet-to-jet variations were attributed to the asymmetric formation of the initial spark kernel inside the pre-chamber, which resulted in asymmetrical distribution of the turbulent jets actuated from six different orifices.

In the context of numerical simulations, a large number of investigations have been performed in parallel to the previously discussed experiments. Starting from simplistic simulations based on unsteady Reynolds Averaged Navier-Stokes (URANS) formulation [25–28] to more sophisticated ones such as Large-Eddy Simulations (LES) [29,19,30] and even Direct Numerical Simulations (DNS) [31–33], multiple researchers have addressed different aspects of the pre-chamber combustion process including the filling process, local flow distribution, flame quenching through the nozzle and the associated composition field. However, it is not easy to establish a direct and quantitative connection based upon such highly sophisticated calculation tools between pre-chamber combustion and the resulting characteristics of the ejected gas jet, which is essentially central for the prediction of the combustion process in the main-chamber. The development of simplified models accounting for the fundamental physics of pre-chamber gas jet ejection and the associated combustion process is an area where contributions are rather scarce [18,34]. In [18] a two-zone model was developed to predict the time evolution of conditions inside the pre-chamber up to the nozzle. However, no link to the ejected gas jet structure was established. In terms of simplified tools, one-dimensional (1-D) models have been successfully utilized for analysis of diesel-type sprays, thereby coupling low computational costs and high prediction capabilities. Especially when boundary conditions are highly controlled, they can deliver an accurate prediction of tip penetration and overall mixing behavior [35–37]. Most of the assumptions used to develop these models are based on turbulent gas jet theory [38]. For example, one of the core simplifications is that the radial spread of axial momentum and mass fraction of the injected stream are self-similar, which reduces the flow to a quasi-steady 1-D problem. Therefore, pre-chamber gas jets are good candidates for the application of these diesel-type spray models. To the best of the authors' knowledge, no direct application of such an approach has been reported in the literature. The availability of such tools with low computational cost would help to bridge the gap between the pre-chamber combustion process and the associated gas jet ejection, which would eventually contribute to a more efficient optimization of this concept for engine applications [23,39,40].

In the present work, pre-chamber spark-ignited engine experiments are conducted in a single-cylinder, heavy-duty, optical engine to characterize the development of turbulent jets and to discuss the role of the ejected flow in the subsequent ignition of the main-chamber mixture. To this end, fuel is only injected in the pre-chamber i.e., no main-chamber fueling is performed, so that the development of the turbulent pre-chamber gas jets into an air ambient can be analyzed without the interference of combustion in the main-chamber. Although some of the previously cited investigations have applied this method with pre-chamber jets ejecting into the main-chamber without any fuel, they only use it as a reference case for the later analysis of a realistic fueling case in the engine, without performing a detailed analysis of the jet dynamics under realistic engine conditions. Cycle-to-cycle and jet-to-jet variations will be the predominant focus of this work. In this study, experimental analysis is supported using a 1-D jet model, which is validated and applied for evaluation of cycle-to-cycle variability in tip penetration. Boundary conditions for the 1-D jet model in terms of mass-flow rate at the nozzle and in-cylinder conditions are estimated based on closed-cycle engine models, including both pre-chamber and main chamber. Both experimental and modeling efforts contribute to the understanding of the relevant phenomena during the pre-chamber ejection process.

## 2. Experimental methods

### 2.1. Optical engine and operating conditions

Experiments are performed in a single-cylinder, heavy-duty optical engine. Visualization is carried out through a Bowditch-type piston with an open, right-cylindrical bowl fitted with a flat fused silica piston-crown window (Fig. 1). The major specifications of the engine are summarized in Table 1, with further details about the facility available elsewhere [41].

Although originally developed as a heavy-duty, optically accessible, single-cylinder diesel engine, it has been suitably modified to operate as a gas engine. The engine is fitted with a pre-chamber spark-ignition module located centrally in the cylinder. The pre-chamber has a volume of $4.66ml$, with 8 equally spaced, $1.6mm$ diameter orifices machined with an included angle of 130°. The pre-chamber tip protrudes $10.6mm$ below the fire deck. The pre-chamber houses a Rimfire Z1 spark plug and a Bosch HDEV5 GDI injector with 6 unequally spaced, $0.17mm$ diameter orifices (Fig. 1). A synthetic mixture comprising 95%$CH_4$, 4%$C_2H_6$ and 1%$C_3H_8$ by volume is used as a surrogate for natural gas.

According to the objective of the study, no fuel is injected at the intake manifold, so that the ejection of pre-chamber jets into an air-ambient can be investigated. The engine is operated at 1200rpm with constant intake conditions ($105kPa$ and $41°C$) such that nominal bulk air conditions of $19bar$ and $730K$ are reached at a spark timing of $343CAD$ (crank angle degree), which is maintained constant. A sweep of air-fuel ratio ($\lambda$) in the pre-chamber (Table 2) has been performed by varying the

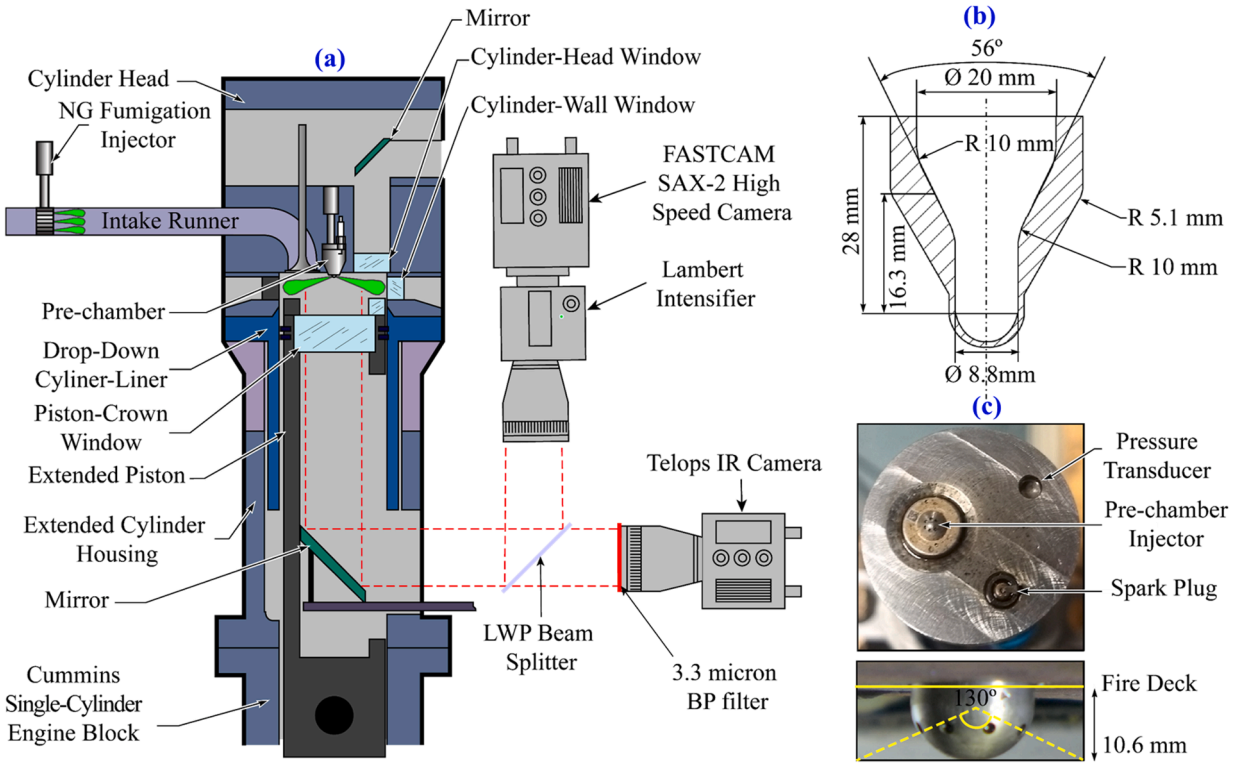


**Fig. 1.** Schematic layout of the (a) optical engine and imaging setup (b) internal geometry of the pre-chamber (c) pre-chamber spark ignition system and its components as installed in the optical engine.

**Table 1**
Major specifications of the single-cylinder optical engine.

| Engine base type | Cummins N-14, DI diesel |
|---|---|
| Displacement [L] | 2.34 |
| Bore x Stroke [cm] | 13.97 x 15.24 |
| Base compression ratio [-] | 11.2 |
| Combustion chamber | Quiescent, direct injection |
| Bowl Width x Depth [cm] | 9.78 x 1.55 |
| Swirl ratio[-] | 0.5 |

**Table 2**
Operating conditions as defined by a $\lambda$ sweep in the pre-chamber along with the corresponding injected fuel mass.

| $\lambda$ [-] | Fuel mass [mg] |
|---|---|
| 1.65 | 1.56 |
| 1.50 | 1.72 |
| 1.25 | 2.06 |
| 1.07 | 2.41 |
| 0.94 | 2.76 |
| 0.83 | 3.10 |
| 0.75 | 3.45 |

start and duration of pre-chamber injector energization, so that a constant timing of 336.6*CAD* for the end of solenoid energization (6.4*CAD* before spark timing) is maintained. Injection pressure is kept constant at 100*bar* throughout the study. Air-fuel ratio values in the table have been calculated by considering the air mass contained in the pre-chamber at spark timing and the total injected fuel mass, since no fuel leakages into the main-chamber can be expected before combustion-induced gas ejection.

The optical engine is operated in a 9 : 1 skip-fire mode, i.e. nine motored cycles precede each fired cycle, which minimizes the amount of residual gases present inside the pre-chamber and the main-chamber clearance volume. This allows for a fundamental study governing the ejection of pre-chamber gas jets avoiding any residual gas effects. Each experimental test run consists of 30 fire cycles after the engine is motored for 60 seconds at constant speed.

### 2.2. Experimental diagnostics

Diagnostics include time-resolved pressure measurements both in the pre-chamber and the main-chamber along with imaging of broadband luminosity in the visible and infrared region. Fig. 1 shows the schematic layout of the optical engine fitted with the pre-chamber spark ignition system along with the imaging setups.

Main-chamber pressure $P_{MC}$ and pre-chamber pressure $P_{PC}$ are measured using an AVL QC34D piezoelectric pressure transducer and an uncooled KISTLER PiezoStar piezoelectric pressure transducer, respectively. Both pressure traces are recorded every quarter crank angle degree. For every fired cycle during which images are acquired, the pressure difference between pre-chamber and main-chamber ($\Delta P = P_{PC} - P_{MC}$) is used extensively for analysis. Furthermore, an apparent heat release rate is calculated based on the whole instantaneous in-cylinder volume, i.e. pre-chamber plus main-chamber [42]. This curve will be used as an input to the modeling approach described later.

Radiation from the main-chamber is imaged through the piston window using a beam splitter arrangement for a two-camera system:

- Broadband visible (VIS) radiation is imaged using a Photron FASTCAM SAX-2 high-speed camera equipped with a Lambert Hi-CATT high-speed intensifier with a S-20 photocathode. This setup records time-resolved images at a 0.5*CAD* resolution with a projected pixel size of 7.5$pix/mm$. The camera effective exposure time is setup by the intensifier gain, which is 50$\mu s$. Due to the absence of soot in this type of combustion, VIS radiation primarily corresponds to

chemiluminescence of products of the pre-chamber combustion being ejected into the main-chamber, or of those species recombining to final products in the main-chamber.

- Infrared (IR) radiation is imaged using a Telops Hyp4 camera equipped with a Spectrogon band-pass filter centered at $3.3\mu m$ with a $215nm$ full width at half-maximum. Due to slow acquisition speed of this camera, it can only acquire only one image per cycle, with a projected pixel size of $4.5pix/mm$. The camera exposure time is $15\mu s$. IR radiation is emitted due to the $C-H$ vibrational stretching of hot unreacted fuel at elevated in-cylinder temperatures caused by compression and/or combustion, or due to the thermal radiation by the hot combustion products emitting VIS radiation.

Due to the difference in the temporal resolution between the two cameras, the experimental methodology has consisted of recording information from 30 fired cycles, for each of which a single IR image, a VIS image sequence and pre-chamber and main-chamber pressure traces are acquired. Image acquisition timing has been suitably adjusted such that every single IR image is simultaneous with one of the VIS images from the 30 acquired sequences. For that purpose, the engine shaft synchronization system has been programmed to send the trigger pulses to both cameras at the specified camera acquisition CAD timings. Fig. 2 shows an example of the acquired information for one fired cycle: A single IR image from that particular cycle, 5 selected VIS snapshots from the recorded VIS sequence along with the corresponding $\Delta P$ signal and the penetration of the pre-chamber gas jets derived from both IR/VIS images. The latter information is obtained by processing the corresponding IR/VIS images using typical Diesel spray processing algorithms as detailed in [36]. Detected contours (colored outlines in Fig. 2) have been overlaid onto the images to improve visualization. Maximum axial extent of the IR/VIS radiation measured from the orifice exit will be referred to as *IR penetration* and *VIS penetration* respectively. Only IR images show the maximum axial-extent (penetration) of the gas jet tip clearly, while VIS images only show a radiation zone that is mostly limited to the near orifice region. Hence, the wording *gas jet penetration* is only appropriate for the IR-derived information. However, confusion will be avoided by using the corresponding IR/VIS acronym.

## 3. Modelling approach

As discussed earlier in the introduction, the aim of this work is to validate a modeling approach that speeds up the design process by predicting gas jet penetration, which has been found to be a governing parameter in pre-chamber combustion. This methodology combines two main tools, a 0-D engine model and a 1-D jet model. Compared to CFD approaches, the main advantage of combining these tools is the fast computation time, which leads to a reduction in the associated computation costs while ensuring a reasonable agreement with experimental results.

A schematic layout of the overall modelling workflow is presented in Fig. 3. Inputs to the 0-D engine model are pressure and temperature at inlet valve closing (IVC), spark timing, injected fuel mass and apparent heat release rate (AHRR). Momentum flux and mass flow rate through the holes are obtained along with the thermodynamic conditions in the main-chamber from the engine modelling part. These results serve as the main inputs for the 1-D jet model, which predicts jet penetration for a single ejected gas jet (S). This modeling workflow can be used on a fully predictive basis, as proposed in [43] by using reasonable assumptions for the AHRR in the pre-chamber. However, the overarching goal of this work is the validation of the whole simulation workflow against experimental data. To this end, experimental AHRR is used as input, while the final predicted pre-chamber gas jet tip penetration profile is compared with the corresponding experimental values.

### 3.1. 0-D Engine model

The engine model is built up within the framework of a commercial 1-D engine modelling software (GT-Power) following the methodology from a previous work [23]. However, in the present case the approach has been simplified to consider only the closed-volume part of the engine cycle, where pre-chamber gas jet ejection and combustion occur. A submodel is implemented for the main-chamber and the pre-chamber, where they are both treated as engine cylinders connected through the pre-chamber orifices with the pre-chamber considered as a non-moving piston. This model reproduces the pressure evolution in both chambers along with the gas exchange between them based on the imposed heat-release rate profile.

Heat release profiles can be imposed either only on the pre-chamber

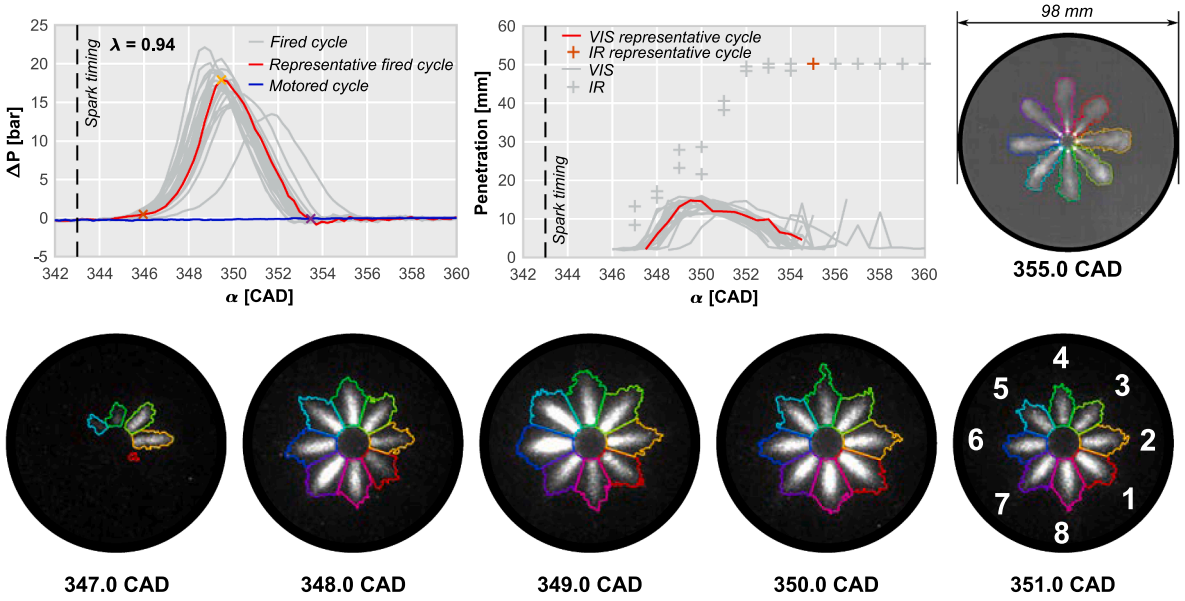


**Fig. 2.** Sample of acquired and processed information from a single fired cycle for $\lambda = 0.93$. Top row: $\Delta P$ (left), IR- and VIS-penetration (middle) and IR image (right)), simultaneous with the VIS image acquired at $349CAD$. Bottom row: Sequence of five VIS images. Overlaid colour lines show detected contours from the image processing algorithm on the corresponding IR/VIS images.

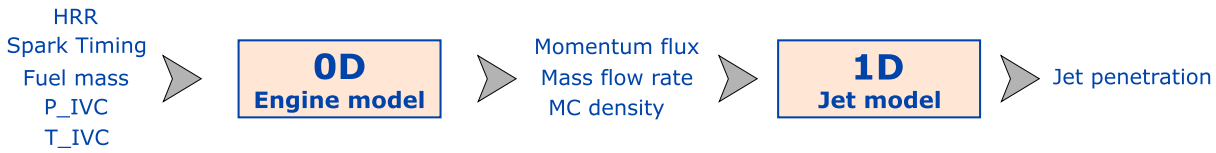


**Fig. 3.** Schematic layout of the modeling workflow coupling the 0-D engine model with the 1-D gas jet model to deliver gas jet tip penetration starting from engine boundary conditions.

or on the main-chamber, or on both of them. The experimental AHRR includes the combined effect of both chemical heat release and heat transfer in the whole main- and pre-chamber volume. However, because of the absence of fuel in the main chamber, the chemical part of AHRR should only be occurring in the pre-chamber. For the simulation part, the chemical part is the one to be imposed only in the pre-chamber. The reconstruction of this chemical part starting from the experimental one is performed in a simplified way, namely the experimental AHRR trace is properly scaled to deliver the fuel energy content in the pre-chamber (fuel mass times lower heating value). Other predictive approaches for the heat-release rate are also feasible, but since the goal of this work is focused on the validation of the workflow, this quasi-diagnostics approach applied here is considered reasonable for our purposes, i.e., a quantitative description of the gas jet flow using the 1-D jet model.

Simulations are carried out into two different steps. The first one consists of a motored cycle, compressing air starting from IVC until the spark timing as set in the experiments. This is followed by a second simulation starting from the start of spark until the end of the cycle. In the second simulation, the fuel-air mass in the pre-chamber is initialized at pressure and temperatures values obtained at the end of the previous simulation. This defines the initial conditions on which the apparent heat-release rate profile is imposed to complete the remaining portion of the closed cycle.

Gas within the pre-chamber is modeled as a perfectly homogeneous mixture with a composition that evolves with time as combustion progresses in a single-zone fashion. Hence, the ejected pre-chamber flow is a mixture of unburned air and fuel, together with burned products ($CO_2$, $H_2O$ and $N_2$), which is indeed a simplification of reality as confirmed by the experimental results. The composition of the burned products is set by considering complete stoichometric combustion. The eight pre-chamber orifices are simulated using a combination of hole and pipe templates. The ejection velocity, mass flow rate and momentum flux from one of the eight orifices is then later used as input for the 1-D gas jet model.

The engine model is calibrated using the experimental data by varying the heat transfer and orifice discharge coefficients until there is reasonable agreement between the simulated and experimental pressure profiles in both the pre-chamber and main-chamber. An example of the calibration results for $\lambda = 0.94$, i.e., experimental (blue) and simulated (orange) pressure profiles is shown in Fig. 4. The light blue area corresponds to the standard deviation in the experimental pressure profiles. Validation results indicate that the 0-D engine model is able to accurately reproduce the experimental pressure trends, thereby making it suitable for our analysis.

### 3.2. 1-D jet model

As discussed earlier in the introduction, one of the main objectives of this work is to validate this modeling approach for the prediction of ejected gas jet penetration. For this purpose, an existing 1-D jet model [37,44–46] is adapted for this application. Although this 1-D jet model has been compared in the past with CFD RANS simulations of gas jets [37,44], most of its applications have been Diesel-like sprays. A detailed description of this model can be found in [37,44] so only the modifications carried out to simulate the gas jets for the pre-chamber configuration are described here:

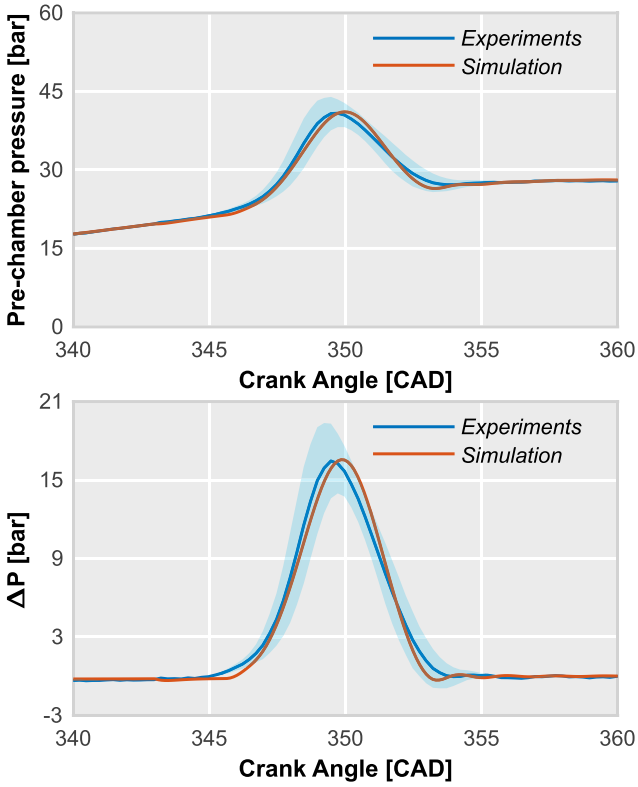


**Fig. 4.** Left: Experimental and simulated pre-chamber pressure profile for $\lambda = 0.94$. Right: Pressure difference ($\Delta P$) between the pre-chamber and main-chamber for the same operating condition.

- An inert configuration is analyzed in this work, i.e., the model describes the turbulent mixing of hot ejected pre-chamber gases with the air ambient in the main-chamber. Although VIS images show some radiation in the vicinity of the pre-chamber nozzle, most of the ejected gas jet volume shows no evidence of chemical activity further downstream of this region.
- The pre-chamber gas jets are modeled as a gas stream injected through the orifices from the pre-chamber into the main-chamber filled with air. Hence, an ideal gas equation of state is used, and a low Mach approach is assumed in terms of compressibility.
- Flow inputs to the 1-D jet model are the time evolution of mass and momentum fluxes through the pre-chamber orifice, which are outputs obtained from the previously described 0-D engine simulations. As opposed to the typical flat top-hat injection profiles used for diesel-like sprays, evolution of such quantities for the pre-chamber configuration is found to be highly transient as shown later.
- While in Diesel-like sprays a cold flow is injected in a hot environment, in this case a stream of a high-temperature fluid (around 1500$K$ based on 0-D engine simulations) from the pre-chamber is ejected into the main-chamber with the ambient at a relatively lower temperature (700$K$). Temperature and mixture composition at the pre-chamber orifice exit are assumed to time-independent (constant) for the sake of simplicity. Since the focus of this work is on

penetration predictions, the most critical parameters are the nozzle momentum flux and ambient density, which govern the jet dynamics. In the most simplified scenario, a non-reacting gas jet could be considered as a constant-density flow [47]; thus, the role of orifice temperature and mixture composition can be effectively ignored.

- Boundary conditions of the main-chamber into which the pre-chamber gas is ejected consists of a time varying density and temperature profile that are also obtained from 0-D engine simulations.
- One of the critical parameters for the application of the 1-D jet model is the radial cone angle, which is often used as a fitting parameter for the experimental tip-penetration data [36]. Here, a constant cone angle of 25° is used. Modelled start of ejection has been shifted for all cases to accommodate for the initial part of ejection process, which is highly challenging to capture in 1-D models due to the uncertainties during the first instants of flow ejection.
- Although interaction between the pre-chamber gas jets and the piston-bowl wall are to be expected in experiments, the 1-D gas jet model only accounts for free-jet propagation.

Fig. 5 shows the predicted $\Delta P$ and the momentum flux at the orifice as derived from the modelling approach as an example of the coupling between the 0-D engine model and the 1-D gas jet one. Main-chamber density is also included, as both momentum flux at the orifice and density of the ambient into which ejection occurs govern the tip penetration of the pre-chamber gas jets, similar to Diesel sprays [44]. Density in the main chamber during the main ejection period is roughly around 11.0–11.5$kg/m^3$ for all conditions, as engine intake conditions are constant in this study. On the other hand, $\Delta P$ is an indicator of the thermal state in the pre-chamber as a result of heat release and it is also the governing parameter for the ejection velocity (and hence momentum) through the pre-chamber holes. Results will evidence the strong relationship between both variables, and hence between pre-chamber combustion and gas jet ejection. Momentum delivery starts when pre-chamber pressure increases as a result of combustion to a value high enough to overcome the cylinder pressure and establish a flow through the orifice. The expected proportionality in the time evolution between both variables ($\Delta P$ and momentum flux) is observed, which also suggests the prominent role of pre-chamber pressure in gas jet ejection, even though compressibility effects might play a role. In terms of $\lambda$ sensitivity, the highest values of peak $\Delta P$ are achieved under fuel-rich conditions ($\lambda = 0.94$), where pre-chamber combustion is fastest, with peak $\Delta P$ values decreasing when moving away from these conditions, specially for the leanest cases.

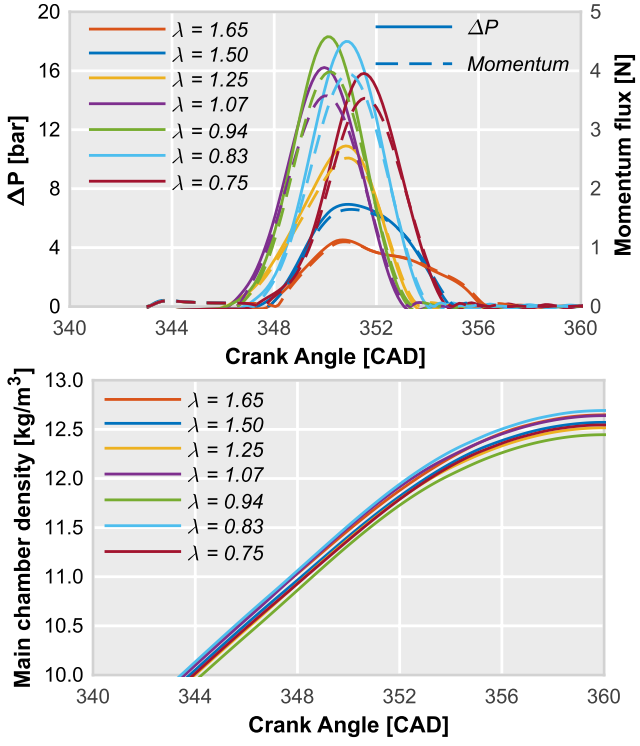


**Fig. 5.** Left: Comparison of the modelled pressure difference $\Delta P$ (solid lines) and jet momentum (dashed lines) for various $\lambda$. Right: Evolution of main-chamber density for various $\lambda$.

## 4. Analysis of pre-chamber combustion cycle-to-cycle variation

### 4.1. Experimental assessment of cycle-to-cycle variation

One of the most prominent features observed in this study has been the cycle-to-cycle variability in the experiments. Fig. 6 shows results that exemplify this phenomenon for $\lambda = 1.50, 0.94, 0.75$. The results are from 30 individual fired cycles along with a *representative cycle* (highlighted in red) identified based on the selection criteria discussed below. Both pressure difference $\Delta P$ between pre-chamber and the main-chamber along with jet tip penetrations from both IR and VIS images are included. High cycle-to-cycle variability is noticeable in all three metrics for both the lean ($\lambda = 1.5$) and rich cases ($\lambda = 0.75$), while this is not so apparent for the near stoichiometric case ($\lambda = 0.94$). In terms of pressure difference, variations influence both the timing of the initial rise, as well as the values of peak $\Delta P$ attained. Variation in timing is also observable in the VIS-based penetration results with similar peak values. As a single IR image is acquired every fired cycle, the cycle to cycle variation cannot be described based upon IR images.

To normalize this timing variability, a so-called 'Start of Ejection' ($SOE_p$) is defined as the crankangle position where the pressure increase ($\Delta P$) exceeds 0.5*bar*. Fig. 7 presents the same results of Fig. 6 but on a $SOE_p$-referenced crankangle basis. From a qualitative perspective, it is clear that the variation in $\Delta P$ decreases significantly especially for the rich case on this modified $SOE_p$-based time referencing. Therefore, it is reasonable to infer that the timing of initial pressure rise within the pre-chamber is most likely to be a major source of the observed cycle-to-cycle variability. However, the overall shape of $\Delta P$ evolution, which dictates the apparent heat-release rate, remains similar. Using the new $SOE_p$-based time-reference also decreases the variations in both IR and VIS-based penetration. Even though cycle-to-cycle variability is lowest for stoichiometric conditions, some IR-based penetration measurements (350*CAD*) are consistently off-trend compared to the adjacent timings. However, when plotted against a $SOE_p$-based crank angle scale, they tend to follow a single consistent trend. Similar to $\Delta P$, all the VIS-based penetration traces are now in phase, with peak penetration values occurring close to the maximum $\Delta P$ timing. This minimization in cycle-to-cycle variation of $\Delta P$ and IR/VIS-based penetration evolution is very evident for the rich case. For the lean case, although the $SOE_p$-based crank angle reference removes the variation in IR/VIS-based penetration for the most part, some spread in the trends is still noticeable. Thus, the cycle-to-cycle variation observed in pre-chamber events for stoichiometric and rich conditions is mainly related to the fluctuations in the start timing of the ejection event. Otherwise, this remains repeatable in terms of both $\Delta P$ and IR/VIS-based penetration.

The earlier analysis revealed a strong link between the pressure difference and the timing of pre-chamber gas jet evolution on a cycle-to-cycle basis. To shed further light on this one-way dependence, Fig. 8 compares the evolution of the start of ejection as derived from the pressure difference ($SOE_p$) to that from VIS images, now defined as the timing of VIS penetration exceeding 5*mm* ($SOE_{VIS}$). The dependence of start of ejection ($SOE_p$ and $SOE_{VIS}$) on $\lambda$ is quite similar for both cases, with the start of ejection reaching minimum values around stoichiometry and increasing with rich and lean mixtures. Another characteristic crank angle position is also plotted in Fig. 8, namely the timing of

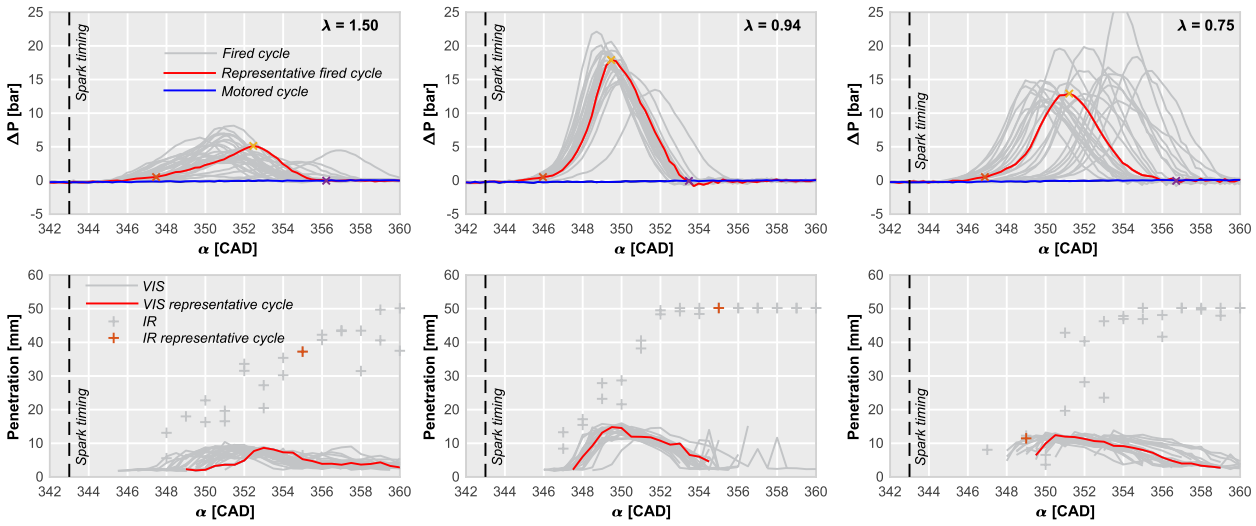


**Fig. 6.** Pressure difference $\Delta P$ between pre-chamber and main-chamber (top) and jet tip penetration (bottom) based on IR (single markers) and VIS (lines) images. $\lambda = 1.50$ (left), 0.94 (middle) and 0.75 (right). Results are from 30 individual fired cycles (gray lines and markers) along with a *representative cycle* (highlighted in red) identified based on the selection criteria discussed in Section 4.1. Vertical dashed line corresponds to the timing of the spark.

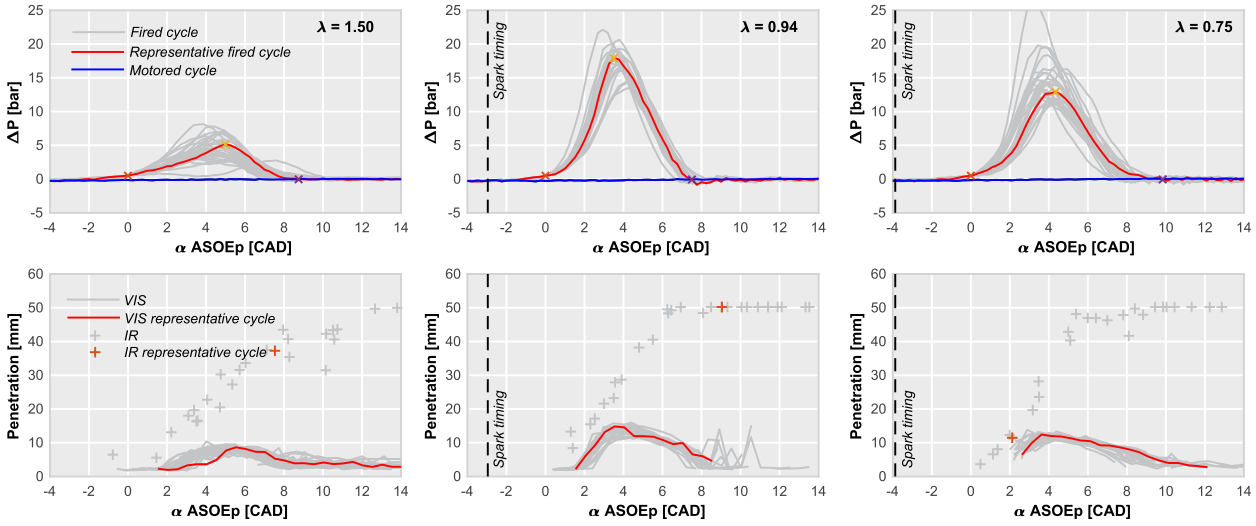


**Fig. 7.** Pressure difference $\Delta P$ between pre-chamber and main-chamber (top) and jet tip penetration (bottom) based on IR (single markers) and VIS (lines) images. $\lambda = 1.50$ (left), 0.94 (middle) and 0.75 (right). Crank angle values are referenced to the start of ejection $SOE_p$ defined based on $\Delta P$ exceeding $0.5bar$. Results are from 30 individual fired cycles (gray lines and markers) along with a *representative cycle* (highlighted in red) identified based on the selection criteria discussed in Section 4.1. Vertical dashed line corresponds to the timing of the spark.

maximum pressure difference $\alpha_{\Delta P_{max}}$, which also exhibits a similar dependency with $\lambda$. Differences between these characteristic timings are almost constant, namely a $2.5°CA$ difference between the two start of ejection definitions and $1.0°CA$ difference between the start of ejection ($SOE_{VIS}$) and $\alpha_{\Delta P_{max}}$. This confirms a stable time sequence of pre-chamber events independent of $\lambda$: starting with the pressure rise in the pre-chamber, followed by the appearance of visible light caused by the ejection of active species and products of combustion from the pre-chamber, leading to maximum pressure difference between the pre-chamber and the main-chamber beyond which the combustion begins to recede.

The peak pressure difference ($\Delta P_{max}$) shown in Fig. 8 can be considered as an indicator of the maximum heat release rate inside the pre-chamber during the combustion process. Compared to the timing evolution, the dependence of $\Delta P_{max}$ on $\lambda$ appears to be reversed, with $\Delta P_{max}$ reaching highest levels at slightly rich conditions, consistent with laminar flame speeds peaking at slightly rich conditions. The magnitude of error bars on the start of ejection timing also indicate that the variation in combustion timing becomes significant at mixture compositions that deviate from stoichiometry. For $\Delta P_{max}$, the absolute variation becomes more pronounced on the rich side, while the relative variation (i.e. the size of the error bar compared to average value) is especially large for lean mixtures. The main conclusion is that the combustion timing in the pre-chamber, the peak pressure difference ($\Delta P_{max}$) and the subsequent ejection processes are strongly dependent on $\lambda$, with fastest and most stable combustion happening around stoichiometry.

Fig. 9 shows the $\Delta P$ profile for individual fired cycles for the same three $\lambda$ values (0.94, 1.5 and 0.75) as analyzed previously with four cycles highlighted: the ensemble-averaged cycle, the single cycles with the maximum and minimum peak pressure difference ($\Delta P_{max}$) and the most *representative cycle* in the sample [48]. The *representative cycle* is defined as the individual cycle that most resembles the average of the samples both in terms of combustion timing and peak pressure difference. In practice, it is chosen as the one cycle that minimizes the merit

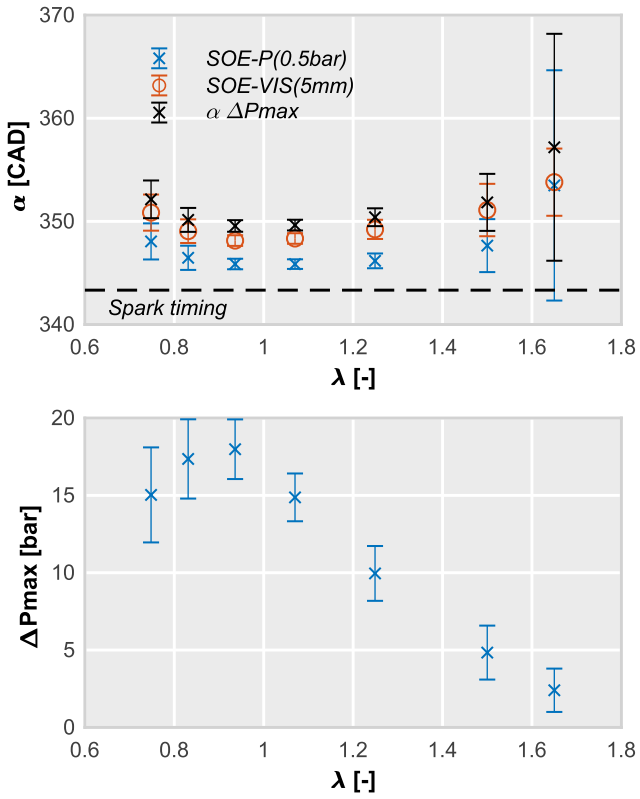


**Fig. 8.** Start of ejection based on $\Delta P$ exceeding 0.5 bar ($SOE_p$) and VIS-based penetration exceeding 5 mm ($SOE_{VIS}$) and the timing of maximum $\Delta P$ (top) and maximum $\Delta P$ values (bottom) for various $\lambda$. Markers indicate the sample-averaged value with error bars corresponding to one standard deviation.

function $f$ in Eq. (1) amongst all cycles in the sample. This merit function for a given jth cycle takes into account the maximum pressure difference ($\Delta P_{max}$) and three characteristic crank angle timings, namely the crank angle of maximum pressure difference ($\alpha_{\Delta P_{max}}$), the start of combustion ($\alpha_{SoC}$) and the end of combustion ($\alpha_{EoC}$) as defined based on the apparent heat-release rate. These variables for every firing cycle are compared against the sample-averaged value of all cycles (denoted by the overbar in Eq. (1)).

$$f^j = \frac{\left|\Delta P^j_{max} - \overline{\Delta P}_{max}\right|}{\overline{\Delta P}_{max}} + \frac{\left|\alpha^j_{\Delta P_{max}} - \overline{\alpha}_{\Delta P_{max}}\right|}{\overline{\alpha}_{\Delta P_{max}}} + \frac{\left|\alpha^j_{SoC} - \overline{\alpha}_{SoC}\right|}{\overline{\alpha}_{SoC}} + \frac{\left|\alpha^j_{EoC} - \overline{\alpha}_{EoC}\right|}{\overline{\alpha}_{EoC}} \tag{1}$$

Though the results in Fig. 9 indicate that the representative cycle is similar to the mean cycle under stoichiometric conditions, where cycle-to-cycle variations remain low, the differences become more evident at lean and rich mixtures. It is precisely this increased spread (dispersion) in the profiles that results in an ensemble-averaged cycle that exhibits a much broader combustion duration with lower $\Delta P_{max}$ values than most cycles in the sample and thereby is not considered representative of the typical combustion evolution. For example, the $\Delta P_{max}$ value for the ensemble-averaged cycle for a rich mixture ($\lambda = 0.75$) is lower than the cycle with minimum $\Delta P_{max}$ values. Thus, the representative cycle based on the function of merit described in Eq. (1) is more appropriate than ensemble averaging to get a realistic evolution of combustion. Corresponding $\Delta P$ profiles and VIS- and IR-based penetration values for this representative cycle have been also highlighted in Figs. 6 and 7.

### 4.2. 1-D modelling analysis of scattering

Since 1-D models usually rely on ensemble-averaged cycle results, they cannot take into account the effect of cycle-to-cycle variability intrinsically. To overcome this caveat, an indirect evaluation of jet tip penetration variability is obtained by running the model with different input values. As described earlier in Section 3.1, the experimental heat release rate is an input parameter to the modeling workflow, which is calculated based on the pressure evolution in the pre-chamber and main-chamber. Our previous analysis has shown that a range of pressure traces ranging from a maximum to a minimum pressure difference between the pre-chamber and main-chamber are obtained. Aside from the ensemble-averaged mean cycle, an experimental cycle, chosen based on a merit function is considered as a good representation of a typical cycle. This section evaluates the variability of the predicted jet tip penetration by feeding these different cycles into the modeling workflow as varying inputs.

Fig. 10 compares the simulated jet tip penetration for each of the four characteristic cycles highlighted in Fig. 9 with the experimental IR-based penetration values, which indicate the tip of the ejected pre-chamber jets. Input momentum fluxes are also included to bridge the link to orifice conditions. The time scale in Fig. 10 is referenced to the start of ejection ($SOE_p$), as this has proven to be a more meaningful way of analyzing the experimental results to shed light on the average behavior of the gas jet independent of its cyclic variability, as discussed in the previous sections. However, it should be noted that this start of ejection ($SOE_p$) time-referencing removes the timing variations in combustion and only considers intensity differences in combustion development for comparison, but the limited temporal resolution of the IR images do not allow for resolving this information on a cycle-to-cycle basis anyways.

The spread (dispersion) in the simulated jet tip penetration values among the different cycles is similar to the observed experimental trend, i.e., the overall prediction is more accurate for stoichiometric and rich cases. The spread is minimum for the stoichiometric condition and especially high for the lean case. If this variation is quantified in terms of jet tip penetration reaching 50*mm* (the limit of the visualization window), it is clear that for the stoichiometric case all cycles reach this value of jet tip penetration within 0.5*CAD* of each other. However, this interval widens to 3.0*CAD* and 4.0*CAD* for the rich and lean cases respectively. In addition to this spread, the predicted jet tip penetration shows good agreement with the experimental values for the ensemble-

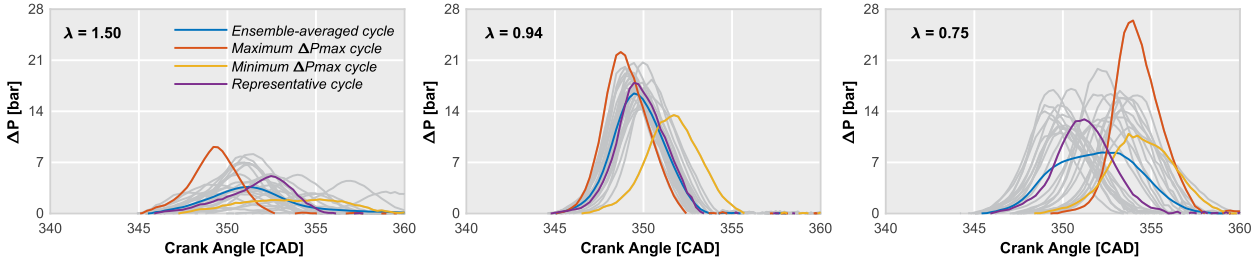


**Fig. 9.** Experimental pressure difference $\Delta P$ for individual cycles and $\lambda = 0.94$, 1.5 and 0.75. Four cycles have been plotted in a different colour, namely the sample mean case, those with the maximum and minimum peak of $\Delta P$ and the representative cycle, which has been obtained as described in the text.

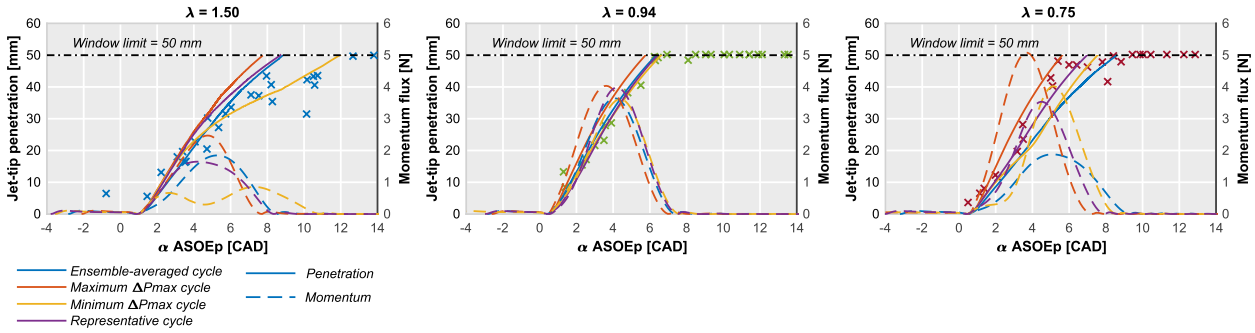


**Fig. 10.** Comparison of jet tip penetration values calculated based on IR images (single markers) with 1-D gas jet simulation results (colored lines). Simulated jet momentum profiles for the four different input cycles (dashed lines) are also shown. Crank angle values are referenced to the start of ejection $SOE_p$ based on $\Delta P$ threshold exceeding $0.5bar$.

averaged cycle only under stoichiometric conditions. For the rich and lean conditions, as the pressure difference (and as a consequence the input heat-release rate) evolution of the ensemble-averaged cycle is much flatter and wider than most of the cycles (c.f. Fig. 9), there is a reduced momentum flux leading to less accurate jet tip penetration prediction results. Again under extreme conditions such as the rich case ($\lambda = 0.75$), the predicted jet tip penetration for the ensemble-averaged cycle is slower than that of the minimum $\Delta P_{max}$ cycle, which is in good agreement with the analysis presented in Fig. 9.

On the other hand, the predicted jet tip penetration evolution for the representative case is in good agreement with the IR-based penetration values for stoichiometric and rich conditions, with the predicted values typically falling between cycles with minimum and maximum $\Delta P_{max}$. However, for the lean case, the agreement is not so good with experimental cycle-to-cycle variations strongly indicating that accurate predictions on a single-cycle basis become increasing difficult due to combustion instability at such lean conditions.

### 4.3. Hole-to-hole variation

In the previous analysis, the image-based start of ejection values have been averaged over all eight of the pre-chamber orifices, however, high-speed VIS images can also be used to discern the jet-to-jet dispersion between pre-chamber jets emanating from different orifices within a single cycle. Low speed acquisition prevents from using IR images for this purposes. Fig. 11 compares the time taken to reach the $5mm$ VIS penetration threshold ($SOE_{VIS}$) for each individual orifice to the orifice-averaged $SOE_{VIS}$ value (both ensemble-averaged over 30 cycles). Negative and positive values for this deviation parameter indicate earlier and later start of ejection respectively for a particular orifice when compared to the orifice-averaged value. In general Fig. 11 shows that a clear gas jet ejection pattern exists in azimuthal direction around the pre-chamber

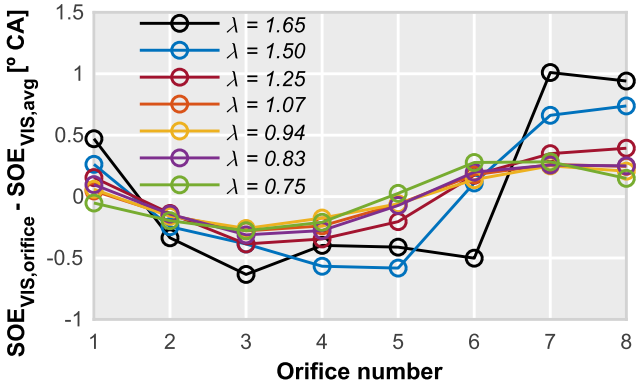


**Fig. 11.** Average deviation of the orifice-resolved start of ejection based on VIS images compared to the sample average one.

axis, with orifices #2 through #5 ejecting earlier than the average (based on images such as those in Fig. 2, orifice #2 corresponds to the 3 o'clock location and the subsequent ones are sequentially numbered in anti-clockwise direction). This sequence is independent of $\lambda$ and is most likely caused by the asymmetry existing inside the pre-chamber due to the location of the spark plug and the injector, which results in a preferential direction for pre-chamber flame propagation towards the faster orifices (#2 - #5). The maximum and minimum dispersion of this deviation parameter around the zero value for a given $\lambda$ indicate the strength of this variation, with results consistently closer to zero and maximum observable dispersion under stoichiometric and lean conditions respectively. Such jet-to-jet dispersion in the pre-chamber gas jet ejection is discussed only in [24], where it is mainly attributed to the asymmetries (non-uniformities) in formation of the initial spark-kernel inside the pre-chamber. Some of the potential factors that contribute to cycle-to-cycle and jet-to-jet dispersion in pre-chamber gas jet ejection are spark kernel repeatability, fuel-air mixture stratification and/ or turbulence inside the pre-chamber. However, since no optical access into the pre-chamber is currently available, one cannot fully discern the true reasons for this behavior using the current engine configuration.

## 5. Analysis of events during pre-chamber gas jet ejection

Fig. 12 shows a representative sequence of composite snapshots for $\lambda = 0.94$, created by superimposing simultaneously acquired IR (employing a red color map) and VIS (employing a green color map) images. This allows to specifically distinguish between regions of burnt gases (stronger IR emission from combustion products) and active chemical reactions (stronger chemiluminescence emission from combustion intermediates) respectively, while describing the overall spatial and temporal evolution of the pre-chamber jets. Due to the selected color scheme, regions of overlap between IR and VIS activity appears in shades of yellow. Acquisition CAD for the images is referenced to both absolute and after start of ejection ($ASOE_p$ defined based on $\Delta P$) based timing based on the individual cycle. The start of ejection based timing reference results in a steadily increasing IR penetration and a fairly cycle-independent $\Delta P$, which helps minimize the effect of cycle-to-cycle variations on the analysis to some extent. Furthermore, the selected operating condition ($\lambda = 0.94$) corresponds to that with the lowest variation as described earlier. Different events can be observed based upon these images:

- Ejection of fresh mixture: The first composite snapshot at $1.4CAD ASOE_p$ shows a preliminary ejection of mass from the pre-chamber. Since only IR signal is observable without any signs of broadband chemiluminescence (only shades of red with no shades of green or yellow), it is most likely that this stems from fresh fuel-air mixture being ejected from the pre-chamber before the premixed flame-front reaches the orifice.

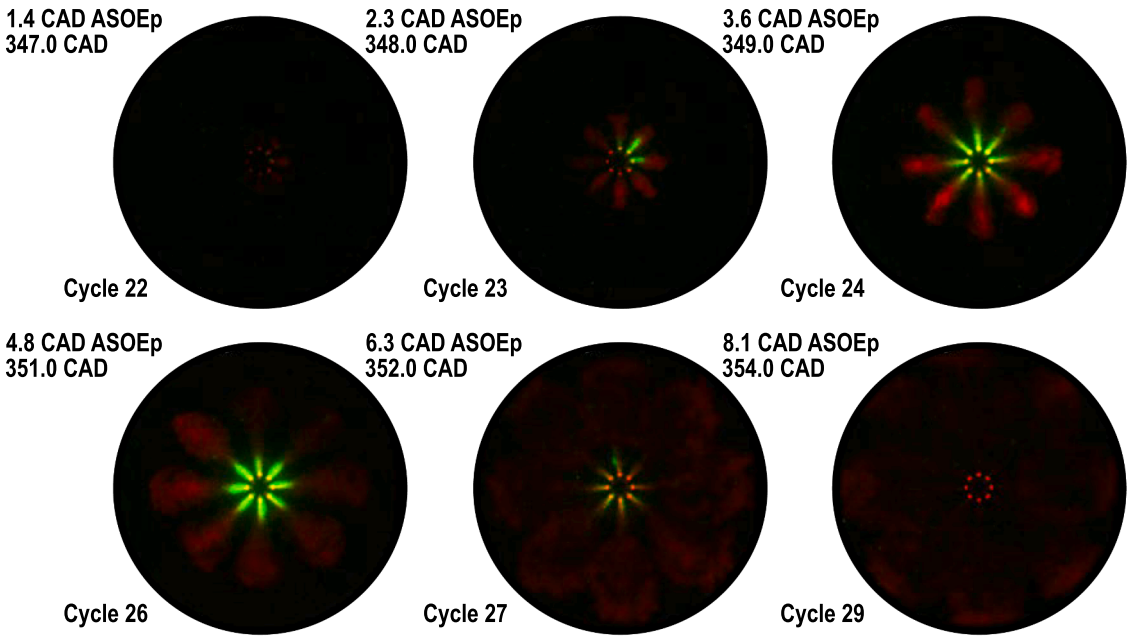


**Fig. 12.** Composite snapshots consisting of simultaneous IR images (red) overlaid on VIS images (green) showing the sequence of events in pre-chamber gas jet ejection for $\lambda = 0.94$. Acquisition CAD (both in absolute terms and after start of ejection ($ASOE_p$) based on $\Delta P$ threshold exceeding $0.5bar$) and acquisition cycle number are indicated on the to-left and bottom-left corner of each image.

- Start of ejection of active products: The second snapshot at $2.3CAD\text{ASOE}_p$ (roughly coinciding with VIS-based start of ejection) shows the first appearance of broadband chemiluminescence i.e., pre-chamber gas jet ejection is discernible from VIS images by means of radiation (greenish regions) in the near-nozzle region, which suggests pre-chamber combustion products reaching the corresponding orifice. As described earlier, there is a clear asymmetry in the initial VIS penetration, with the 3 o'clock and the adjacent jet in the anti-clockwise direction (#2 and #3 respectively) already penetrating until roughly $10mm$, while no luminosity is observable in other orifices. The IR signal extends further away from the pre-chamber nozzles indicating that the initially ejected fuel-air mixture reaches deep into the main-chamber. The corresponding IR-based jet tip penetration is significantly longer than the VIS-based value, with a much more symmetrical layout. The observed symmetry in the IR imaging confirms that the IR jets initially correspond to fresh unreacted fuel-air mixture being forced through the pre-chamber orifices, which is mainly governed by the pressure difference P, thereby resulting in minimal jet-to-jet variation,
- Peak pressure increase: The third composite snapshot at $3.6CAD\text{ASOE}_p$ corresponds to the timing of maximum VIS penetration and roughly maximum $\Delta P_{max}$ between the pre-chamber and main-chamber. The overall appearance of the pre-chamber jets is fairly similar to the previous snapshot, but with IR signal penetration progressing further into the main-chamber. The main difference between the two snapshots is in the near-orifice region, where VIS luminosity is almost symmetrical extending from the eight pre-chamber orifices. The axial extent of the VIS region at this instant is around $11mm$ and is consistent for all pre-chamber orifices. This potentially indicates that conditions upstream of the orifices are similar, i.e., the premixed flame-front has most likely consumed all the available fuel-air mixture in pre-chamber.
- Piston window impingement: The fourth composite snapshot at $4.8CAD\text{ASOE}_p$ corresponds to around $1CAD$ after maximum pressure difference ($\Delta P_{max}$) for that particular cycle is attained. This indicates that the combustion in the pre-chamber is receding, i.e., heat-release cannot compensate for the ejection of gas and heat transfer to the surroundings leading to decreasing $\Delta P$. Again, a similar overall pre-chamber gas jet structure is observable based on the IR and VIS images, with a very intense VIS radiation. However, the IR radiation at the jet tip appears wider when compared to the earlier snapshots. As no IR luminosity change is observable in this region, no additional heat-release is to be expected, i.e., there is no evidence of the initially unreacted fuel-air mixture igniting and undergoing combustion. Hence, this widening of the pre-chamber gas jet head cannot be due to combustion, as in a diesel-jet after ignition [45]. Instead, this radial widening of the jet tip appears to be consistent with the gas jet impinging on the piston window, which is confirmed by comparing the IR-based jet tip penetration with the position of the bowl window at that timing.
- End of ejection: The last two composite snapshots at 6.3 and $8.1CAD\text{ASOE}_p$ correspond to later stages when the pressure difference $\Delta P$ drops back to zero. The intensity of gas jet radiation in both VIS and IR is significantly lower than the earlier snapshots. This is especially evident in the VIS region, where radiation primarily stems from chemically reacting products being ejected through the nozzle orifices, which are depleted by the end of pre-chamber combustion process. VIS radiation eventually disappears, while the IR signal extends further in the form a wall gas jet along the piston window towards the cylinder wall. The jet structure essentially vanishes in the last snapshot, where the injected mass appears to be spread across the entire main-chamber. In this particular instant, the radiation at the exit of the pre-chamber orifice is clearly visible, which is most likely caused by thermal radiation emanating from the hot mass remaining within the pre-chamber and/ or hot surfaces inside the pre-chamber.

Fig. 13 and 14 show similar sequence of composite snapshots for a rich ($\lambda = 0.75$) and lean ($\lambda = 1.50$) condition respectively. The rich case appears fairly similar to the stoichiometric one discussed earlier in terms of the sequence of events, observed gas jet radiation structure and spatial evolution of the pre-chamber gas jets during the ejection process. Note that in the rich case, it is reasonable to expect some chemical activity extending in the downstream direction, due to the excess fuel in the pre-chamber possibly being oxidized by the air in the main-chamber. However, the IR images do not show any indication of strong radiation

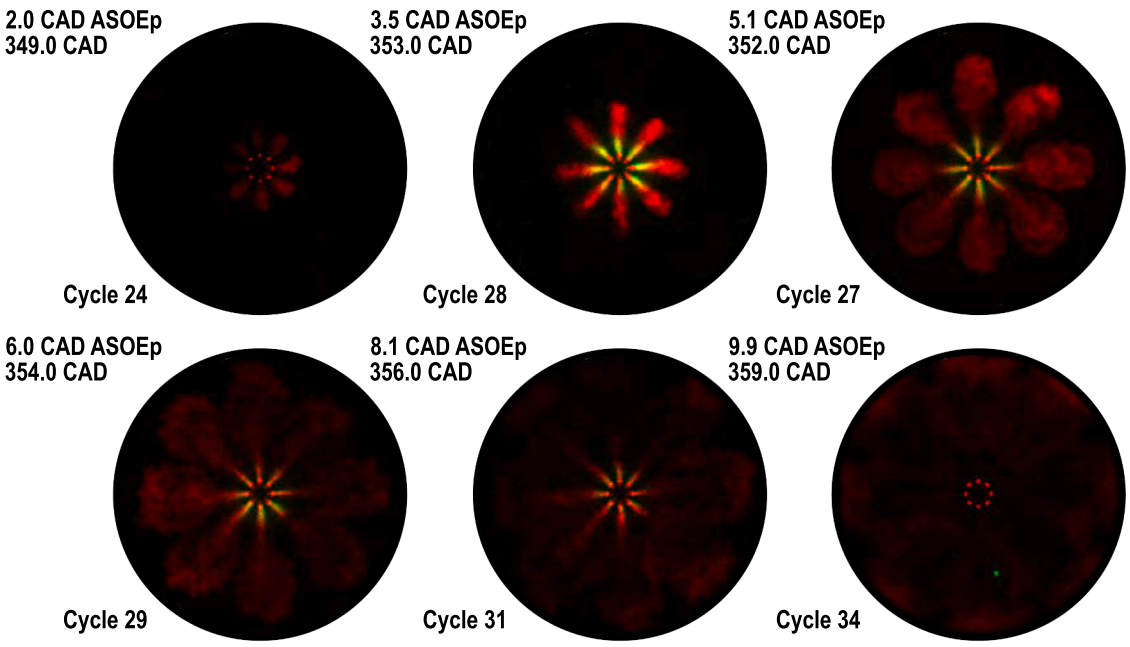


**Fig. 13.** Composite snapshots consisting of simultaneous IR images (red) overlaid on VIS images (green) showing the sequence of events in pre-chamber gas jet ejection for $\lambda = 0.75$. Acquisition CAD (both in absolute terms and after start of ejection ($ASOE_p$) based on $\Delta P$ threshold exceeding 0.5*bar*) and acquisition cycle number are indicated on the to-left and bottom-left corner of each image.

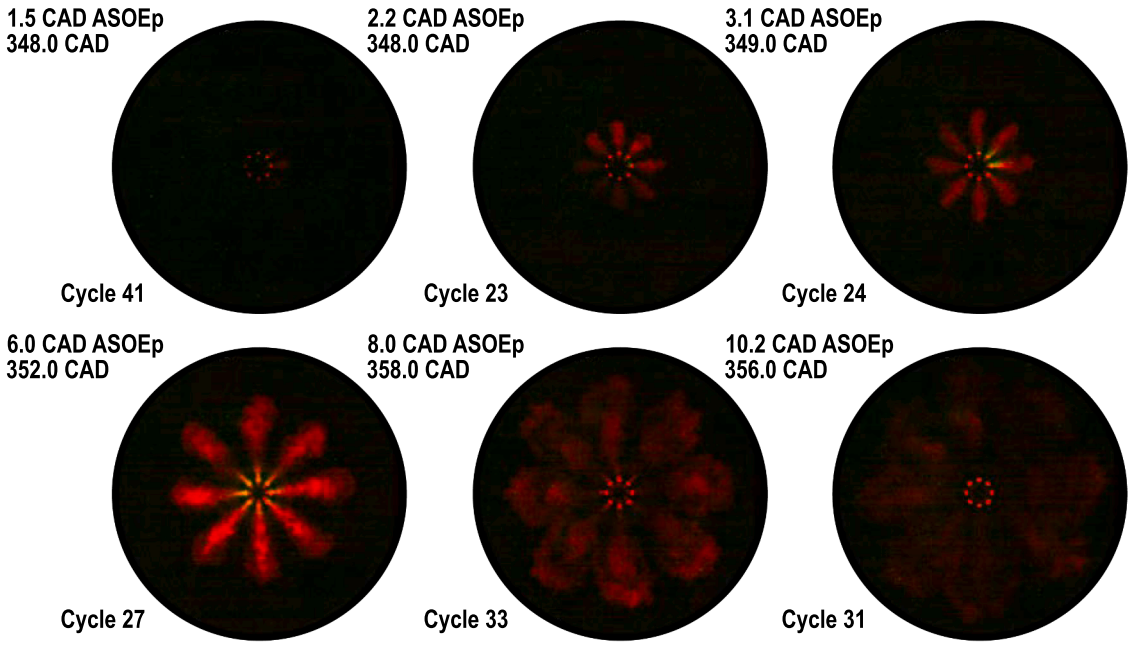


**Fig. 14.** Composite snapshots consisting of simultaneous IR images (red) overlaid on VIS images (green) showing the sequence of events in pre-chamber gas jet ejection for $\lambda = 1.50$. Acquisition CAD (both in absolute terms and after start of ejection ($ASOE_p$) based on $\Delta P$ threshold exceeding 0.5*bar*) and acquisition cycle number are indicated on the to-left and bottom-left corner of each image.

at the jet tip, which would possibly indicate local heat release and subsequent temperature rise. The 1-D gas jet model will be used to show that as the gas jet penetrates further downstream of the nozzle, the increasing air entrainment strongly dilutes the ejected mass to mixtures that are too lean to support combustion. This suggests that ambient entrainment plays a leading role in the evolution of the ejected combustion products.

As for the lean case, the sequence of events remains consistent but with much lower VIS radiation levels due to the less intense heat release associated with lean combustion. The ejected combustion products from a lean mixture will be significantly different in composition when compared to the other two cases. Furthermore, the lower pressure difference results in lower gas jet momentum at the nozzle leading to a shorter penetration of the gas jet, as modeling will confirm.

### 5.1. 1-D Modeling analysis of the gas jet ejection process

Fig. 15 summarizes 1-D modeling results of jet tip penetration for all

operating conditions in this study. Only 1-D model predictions based upon the representative cycle are shown with predicted jet tip penetration values compared to experimental IR- and VIS-based results. The IR-based jet tip penetration values are plotted for all 30 cycles, while only the representative cycle is included for the VIS-based information. Starting with the leanest case, the trends clearly show that IR-based jet tip penetration becomes faster with richer pre-chamber conditions down to $\lambda = 0.94$. The remaining rich cases show very similar jet tip penetration results though the peak momentum slightly decreases, which is in good agreement with the measured peak $\Delta P$ values shown in Fig. 8.

The agreement of the predicted 1-D modeling based jet tip penetration values with the IR-based results is good starting from $\lambda = 1.25$ and into the richer conditions. For the leanest of the conditions, accuracy is just fair. An almost 1*CAD* shift between the initial timing of the penetration based on the modeling and experimental results is also observable with the three leanest cases. For these cases, the spread in experimental data is evident, which indicates that combustion is more unstable not just in timing but also in development, hence generating reliable modeling predictions becomes far more difficult. For the other stoichiometric and rich conditions, the agreement between the modeling and experimental results is quite remarkable.

Fig. 16 provides further insight into the evolution of flow dynamics along the gas jet axis during the ejection process for $\lambda = 0.94$ using the representative engine cycle. Corresponding momentum flux at the nozzle and the modeled gas jet tip penetration have been presented earlier in Fig. 10. Mass and momentum fluxes along the gas jet axial coordinate at different instances during the ejection process are shown with colors signifying the crank angle timing. To facilitate analysis, plots are split into two intervals corresponding to timings before and after the occurrence of maximum momentum flux. During the initial stage of the ejection process (left plots in Fig. 16), both momentum flux and mass flow increase with time as expected. A gas jet can be considered as a set of momentum flux parcels that travel downstream incorporating ('entraining') ambient gas, which is quantified in terms of the mass flux. At any given instant, the momentum flux decreases with the axial distance as the parcels with the highest momentum are the latest injected ones, which are much closer to the orifice. Such parcels tend to push the ones ahead thereby transferring momentum towards the jet tip. On the other hand, mass flux at any given instant is always increasing with axial distance as the entrainment of ambient mass from the main-chamber starts at the nozzle and increases with the parcel timeline, i.e. along the axial distance. This means that the ejected pre-chamber gas jet flow becomes increasingly diluted with axial distance.

Consistent with the previous description of the gas jet, the later ejected parcels (right plots in Fig. 16) have lower momentum than the ones ejected earlier. Hence, starting from the earlier slightly decreasing axial distribution, the shape of the momentum flux progressively turns into an increasing function. This means that the newly injected parcels do not help in pushing the jet tip anymore. As for the mass flux, the axially-increasing trend remains the same during the second phase, as ambient mass is steadily being incorporated into the spray due to the momentum flux. However, mass flux values at a given axial position steadily decrease with time, although the temporal decrease rate is much lower than that of the momentum flux. This evolution is similar to the end of injection event in diesel-like sprays, investigated in detail in [35]. Owing to the decreasing momentum flux, progress in jet tip penetration in the second phase is roughly only 15*mm* compared to the initial increase of more than 30*mm* during the first phase of the pre-chamber gas jet ejection process.

Fig. 17 compares the magnitudes of mass and momentum fluxes for three operating conditions, namely $\lambda = 1.55$, 0.94and 0.75 at two characteristic timings, namely during the occurrence of peak momentum flux at the orifice (last timing on Fig. 16, left) and at the end of ejection (last timing on Fig. 16, right). The previously observed trends for momentum and mass flux distribution along the spray axis remain relatively similar for all three operating conditions at both timings. During the maximum momentum flux timing at the orifice, the results clearly indicate higher local momentum and mass fluxes for the stoichiometric condition compared to the other conditions, due to the more rapid pre-chamber combustion development. A higher momentum flux leads to more intense entrainment of ambient air and hence increased mass flow.

Entrainment effects are also estimated in terms of a third variable shown on the plot, namely the air-fuel ratio $\lambda_{cl}$ along the gas jet axis. This will be the richest location within the jet cross-section at each axial position of the gas jet, as the fuel mass fraction profiles are assumed to follow a Gaussian distribution in the 1-D model. In the near-orifice region, the local value of $\lambda_{cl}$ correlates to the corresponding pre-chamber $\lambda$

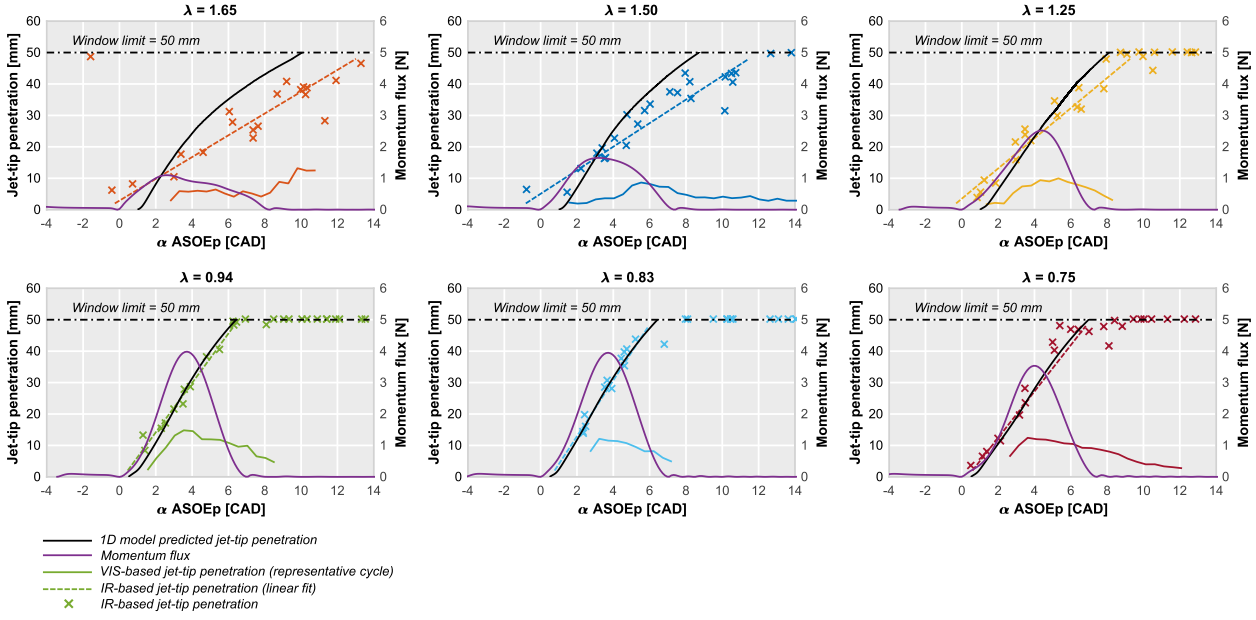


**Fig. 15.** Comparison of jet tip penetration based on IR (single markers - all cycles, dotted line - linear fit) and VIS (colored line - only representative cycle) imaging with predicted jet tip penetration values (black line) using the input data from the representative cycle. Momentum flux used for the simulation is also included. Crank angle values are referenced to the start of ejection $SOE_p$ based on $\Delta P$ exceeding 0.5*bar*.

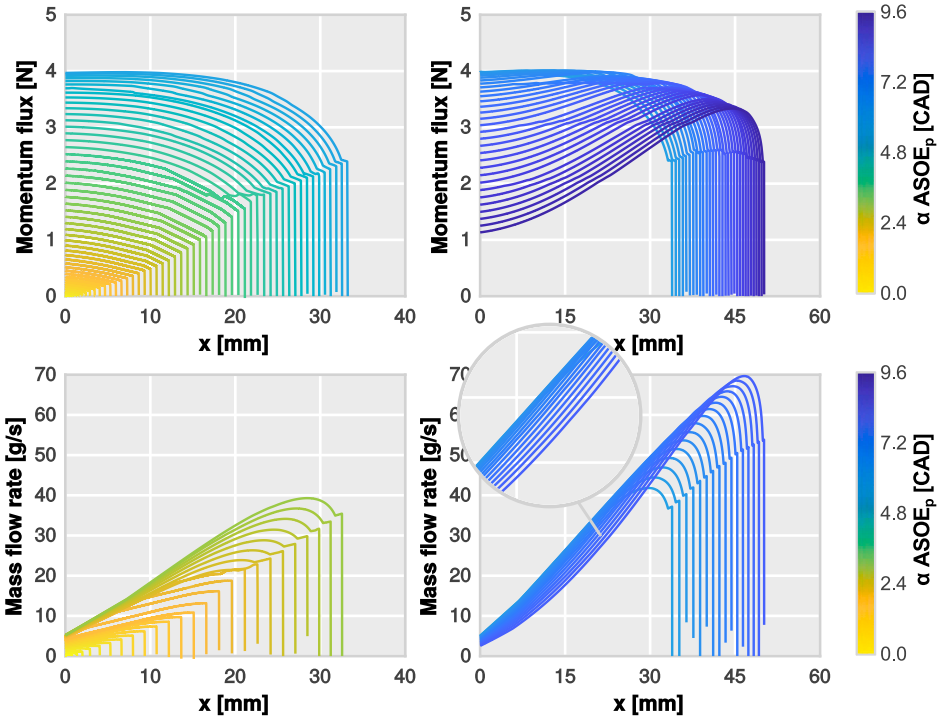


**Fig. 16.** Spatial distribution of momentum (top) and mass fluxes (bottom) along the axial coordinate of the gas jet at different instances during pre-chamber gas jet ejection process for $\lambda = 0.94$ using the representative cycle. Colored contours correspond to different timings indicated by CAD values after $SOE_p$ as shown by the color bar. Plots on the left correspond to timings between start of ejection and the occurrence of maximum momentum flux, while plots on the right correspond to subsequent timings until the end of ejection.

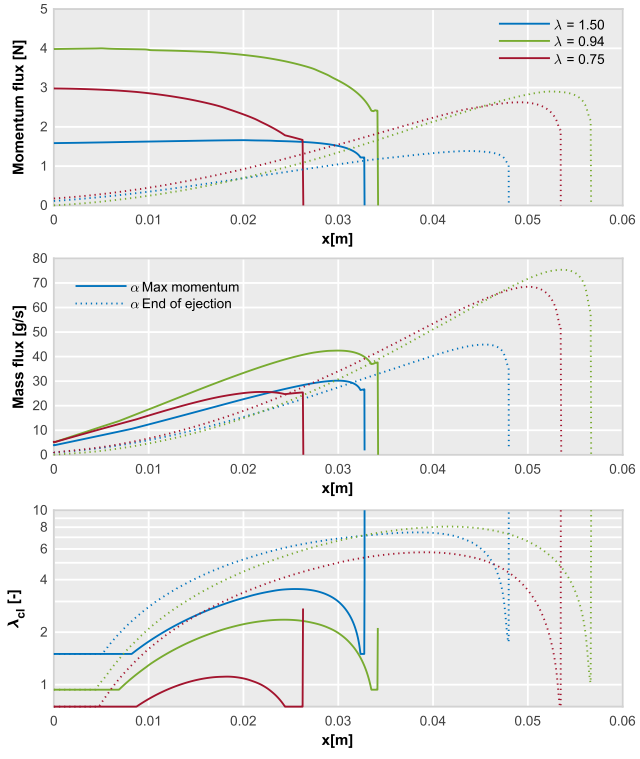


**Fig. 17.** Spatial distribution of momentum (top) and mass fluxes (middle), as well as air-excess ratio $\lambda_{cl}$ (bottom) along the axial coordinate of the gas jet for $\lambda = 1.55$, 0.94 and 0.75 using the representative cycle. Timings correspond to the instance of maximum momentum flux (solid line) and the end of ejection (dashed line).

value, and increases after remaining constant for a short distance. Beyond this region, the stoichiometric pre-chamber condition exhibits the most prominent increase in $\lambda_{cl}$ up to around 15*mm*, indicating faster entrainment; despite this, it never reaches $\lambda_{cl}$ values associated with the leanest condition. Furthermore, none of the three shown $\lambda_{cl}$ evolution intersect with each other. The decreasing trend observed at the tip of the jet is an artifact of the 1D simplification of the jet tip zone, which is specially evident for highly transient injection velocity, as already shown in [37].

At the end of ejection timing, results show that the spray tip propagates with larger momentum for the stoichiometric condition compared to the other two. However, distribution of mass and momentum fluxes remain fairly similar for all three conditions starting from the orifice exit up to around 30*mm* downstream. This indicates that the second phase of gas jet ejection (following the occurrence of peak momentum flux) results in a very similar flow state near the vicinity of the pre-chamber orifice at the end of the ejection process. In other words, the initial ramp-up period of ejection until the occurrence of maximum momentum flux is the most dependent on pre-chamber combustion characteristics. For scenarios with fuel-air mixtures present in the main-chamber, the subsequent combustion development is most likely to be influenced by this initial ejection phase, as the ramp-down phase of ejection collapses to very similar flow distributions, almost independent of the operating conditions.

Information derived from the 1-D model analysis also provides a rough quantification for the dilution of the ejected pre-chamber gases. As seen from the experimental images, there is no evidence of chemical activity in regions situated further downstream of the maximum VIS penetration length (8 to 15*mm* depending on $\lambda$). According to the estimations of the 1-D model, the richest locations within the gas jet at the timing of maximum momentum flux will all be below a local $\lambda = 2$ for distances longer than 15*mm*, except for the stoichiometric case. At the end of ejection timing, the plot shows all conditions being much leaner than the $\lambda = 2$. Keeping in mind that most of the ejected mass will be leaner than the values shown on the spray axis, the resulting mixture is most likely too lean to react, which is in agreement with the absence of chemical activity in the experimental images downstream of the maximum VIS penetration.

## 6. Summary and conclusions

This work reports an experimental study of pre-chamber gas jets

ejected into the main-chamber (air ambient) in a heavy-duty, single-cylinder optical engine. This pre-chamber only fueling strategy eliminates the effect of ignition and subsequent combustion development in the main-chamber on pre-chamber gas jet flow dynamics. Different objectives have been achieved, namely the detailed description of the near-orifice hot jets structure by means of high-speed visible imaging, the quantification of the tip penetration by means of low speed infrarred imaging, a detailed analysis of cycle-to-cycle scattering as well as the validation of a 1-D gas jet model to describe the ejected gas flow dynamics.

The main conclusions of this study are summarized as follows:

- Cycle-to-cycle variation in the ejection process is quantified in detail in terms of both pressure difference and jet-penetration. As expected, stable combustion is achieved around stoichiometric conditions due to rapid heat-release.
- Although cycle-to-cycle variations are linked to maximum burning rate and thereby to the peak pressure in the pre-chamber, most of the observed fluctuations tend to disappear when referencing the time evolution to the start of ejection, which is defined based on a threshold pressure difference of $0.5bar$ or a visible radiation penetration threshold of $5mm$. Thus, most of the fluctuations are related to the start of combustion in the pre-chamber. Jet-to-jet variations shows a repeatable ignition sequence with some orifices ejecting earlier than others do. This most likely stems from the differences in the dynamics of premixed flame-front propagation within the pre-chamber. This is most likely due to the intense turbulence induced stratification of the pre-chamber charge caused by the fuel injection event and the stochastic nature of ignition event, but further investigation is warranted to confirm this hypothesis.
- Combustion evolution is described using visible and infrared images. Ejection of unreacted fresh fuel-air mixture into the main-chamber is detected from infrared images initially due to the favorable pressure drop across the orifice. Visible radiation is detected only after a delay (typically in the order of $2.5CAD$) from the start of ejection as defined in terms of pressure difference ($\Delta P$). This chemiluminescence activity is limited exclusively to the vicinity of the orifice, while downstream of this region only infrared radiation is observable. No indication of chemical activity is detectable in the infrared-only region, which is most likely due to the ultra-lean mixture composition (no fueling of the main-chamber).
- A 1-D spray model is adapted to predict tip-penetration of ejected pre-chamber gas jets. Flow conditions at the orifice (mass and momentum fluxes) are obtained using a 0-D analysis of the pre-chamber and main chamber. Time-varying ambient conditions in the pre-chamber are also obtained from the 0-D analysis.
- Variation in the tip-penetration is quantified based on 1-D model predictions with different input data derived from corresponding experimental runs. Conditions of sample mean pressure rise along with extreme values (maximum and minimum) of pressure increase are evaluated along with a *representative cycle*, selected based on a merit function. The representative cycle case provides most accurate predictions of tip-penetration, while the sample mean case performs poorly especially in conditions with significant cycle-to-cycle variation. Hence, the proposed 1-D computational tool can be used for pre-chamber gas jet tip-penetration predictions with reasonable certainty. ‘
- Analysis of the 1-D jet model predictions suggests that the initial ejection process, i.e., until the point of maximum momentum flux at the nozzle, is highly dependent on the air-fuel ratio $\lambda$ in the pre-chamber. Hence, the local flow and most likely the associated combustion development for fuelled main-chamber scenario will be highly dependent on this early-ejection phase. Flow evolution at later timings becomes relatively independent of $\lambda$ in the pre-chamber, with a characteristic fast slow-down due to the steeply decreasing ejection velocities.

## CRediT authorship contribution statement

**J.M. García-Oliver:** Conceptualization, Formal analysis, Investigation, Data curation, Visualization, Writing - original draft. **Y. Niki:** Conceptualization, Formal analysis, Investigation, Data curation, Writing - review & editing. **R. Rajasegar:** Conceptualization, Formal analysis, Investigation, Data curation, Visualization, Writing - review & editing. **R. Novella:** Conceptualization, Formal analysis, Writing - original draft. **J. Gomez-Soriano:** Conceptualization, Formal analysis, Data curation, Visualization, Writing - original draft. **P.J. Martínez-Hernándiz:** Conceptualization, Formal analysis, Data curation, Visualization, Writing - original draft. **Z. Li:** Conceptualization, Investigation, Writing - review & editing. **M.P.B. Musculus:** Conceptualization, Formal analysis, Investigation, Resources, Project administration, Writing - review & editing.

## Declaration of Competing Interest

The authors declare that they have no known competing financial interests or personal relationships that could have appeared to influence the work reported in this paper.

## Acknowledgements

This research was sponsored by the U.S. Department of Energy (DOE) Office of Energy Efficiency and Renewable Energy (EERE). Optical engine experiments were conducted at the Combustion Research Facility, Sandia National Laboratories, Livermore, CA. Sandia National Laboratories is a multi-mission laboratory managed and operated by National Technology and Engineering Solutions of Sandia, LLC., a wholly owned subsidiary of Honeywell International, Inc., for the U.S. Department of Energy’s National Nuclear Security Administration under contract DE-NA0003525.

José M García-Oliver acknowledges the support of the Generalitat Valenciana government in Spain through Grant Best/2019/176 for his scientific visit to the Combustion Research Facility. P. J. Martínez-Hernándiz is partly supported by an FPI contract (FPI-S2-19-21993) of the “Programa de Apoyo para la Investigación y Desarrollo (PAID-05–19)” of the Universitat Politécnica de Valéncia.

## References

[1] Heyne S, Meier M, Imbert B, Favrat D. Experimental investigation of prechamber autoignition in a natural gas engine for cogeneration. Fuel 2009;88(3):547–52. https://doi.org/10.1016/j.fuel.2008.09.032.
[2] Jamrozik A. Lean combustion by a pre-chamber charge stratification in a stationary spark ignited engine. J Mech Sci Technol 2015;29(5):2269–78. https://doi.org/10.1007/s12206-015-0145-7.
[3] Benajes J, Novella R, Gomez-Soriano J, Barbery I, Libert C, Rampanarivo F, Dabiri M. Computational assessment towards understanding the energy conversion and combustion process of lean mixtures in passive pre-chamber ignited engines. Appl Thermal Eng 2020;178:115501. https://doi.org/10.1016/j.applthermaleng.2020.115501.
[4] Hlaing P, Echeverri Marquez M, Singh E, Almatrafi F, Cenker E, Ben Houidi M, Johansson B. Effect of pre-chamber enrichment on lean burn pre-chamber spark ignition combustion concept with a narrow-throat geometry. WCX SAE World Congress Experience 2020. https://doi.org/10.4271/2020-01-0825.
[5] A. Shah, Improving the efficiency of gas engines using pre-chamber ignition, Ph.D. thesis, Lund University (2015).
[6] Toulson E, Schock HJ, Attard WP. A review of pre-chamber initiated jet ignition combustion systems. SAE 2010 Powertrains Fuels & Lubricants Meeting 2010. https://doi.org/10.4271/2010-01-2263.
[7] Shah A, Tunestal P, Johansson B, Effect of relative mixture strength on performance of divided chamber ’avalanche activated combustion’ ignition technique in a heavy duty natural gas engine, SAE 2014 World Congress & Exhibition 2014–01-1327. doi: 10.4271/2014-01-1327.
[8] Attard WP, Bassett M, Parsons P, Blaxill H. A new combustion system achieving high drive cycle fuel economy improvements in a modern vehicle powertrain. SAE 2011 World Congress & Exhibition 2011. https://doi.org/10.4271/2011-01-0664.
[9] Pan J, Hu Z, Wei H, Pan M, Liang X, Shu G, Zhou L, Understanding strong knocking mechanism through high-strength optical rapid compression machines, Combustion and Flame 202 (2019) 1–15. doi:https://doi.org/10.1016/j.combustflame.2019.01.004.

[10] Chen C, Pal P, Ameen M, Feng D, Wei H, Large-eddy simulation study on cycle-to-cycle variation of knocking combustion in a spark-ignition engine, Applied Energy 261 (2020) 114447. doi:https://doi.org/10.1016/j.apenergy.2019.114447.
[11] Broatch A, Novella R, García-Tíscar J, Gomez-Soriano J, Pal P. Investigation of the effects of turbulence modeling on the prediction of compression-ignition combustion unsteadiness. Int J Engine Res 2021;1468087421990478.
[12] Attard WP, Blaxill H. A gasoline fueled pre-chamber jet ignition combustion system at unthrottled conditions. SAE Int J Engines 2012;5(2):315–29. https://doi.org/10.4271/2012-01-0386.
[13] Alvarez CEC, Couto GE, Roso VR, Thiriet AB, Valle RM. A review of prechamber ignition systems as lean combustion technology for si engines. Appl Thermal Eng 2018;128:107–20. https://doi.org/10.1016/j.applthermaleng.2017.08.118.
[14] Natural gas vehicle research workshop, U.S. Department of Energy - Vehicle Technologies Office, 2017.
[15] Yamaguchi S, Ohiwa N, Hasegawa T. Ignition and burning process in a divided chamber bomb. Combustion Flame 1985;59(2):177–87. https://doi.org/10.1016/0010-2180(85)90023-9.
[16] Biswas S, Tanvir S, Wang H, Qiao L. On ignition mechanisms of premixed ch4/air and h2/air using a hot turbulent jet generated by pre-chamber combustion. App Thermal Eng 2016;106:925–37. https://doi.org/10.1016/j.applthermaleng.2016.06.070.
[17] Biswas S, Qiao L. Ignition of ultra-lean premixed hydrogen/air by an impinging hot jet. Appl Energy 2018;228:954–64. https://doi.org/10.1016/j.apenergy.2018.06.102.
[18] Mastorakos E, Allison P, Giusti A, De Oliveira P, Benekos S, Wright Y, Frouzakis C, Boulouchos K. Fundamental aspects of jet ignition for natural gas engines. SAE Int J Eng 2017;5(10):2429–38. https://doi.org/10.4271/2017-24-0097.
[19] Allison P, de Oliveira M, Giusti A, Mastorakos E. Pre-chamber ignition mechanism: Experiments and simulations on turbulent jet flame structure. Fuel 2018;230:274–81. https://doi.org/10.1016/j.fuel.2018.05.005.
[20] Gentz G, Thelen B, Litke P, Hoke J, Toulson E. Combustion visualization, performance, and cfd modeling of a pre-chamber turbulent jet ignition system in a rapid compression machine. SAE Int J Eng 2015;8(2):538–46. https://doi.org/10.4271/2015-01-0779.
[21] M. Gholamisheeri, B.C. Thelen, G.R. Gentz, I.S. Wichman, E. Toulson, Rapid compression machine study of a premixed, variable inlet density and flow rate, confined turbulent jet, Combustion and Flame 169 (2016) 321 – 332. doi:https://doi.org/10.1016/j.combustflame.2016.05.001.
[22] Schlatter S, Schneider B, Wright YM, Boulouchos K. Comparative study of ignition systems for lean burn gas engines in an optically accessible rapid compression expansion machine. 11th International Conference on Engines & Vehicles 2013–24-0112.. https://doi.org/10.4271/2013-24-0112.
[23] J. Benajes, R. Novella, J. Gomez-Soriano, P. Martinez-Hernandiz, C. Libert, M. Dabiri, Evaluation of the passive pre-chamber ignition concept for future high compression ratio turbocharged spark-ignition engines, Applied Energy 248 (2019) 576 – 588. doi:https://doi.org/10.1016/j.apenergy.2019.04.131.
[24] Li X, Zhang W, Huang Z, Ju D, Huang L, Feng M, Lu X, Huang Z. Pre-chamber turbulent jet ignition of methane/air mixtures with multiple orifices in a large bore constant volume chamber: effect of air-fuel equivalence ratio and pre-mixed pressure. Frontiers Energy 2019;13(3):483–93. https://doi.org/10.1007/s11708-019-0631-1.
[25] A. Shah, P. Tunestal, B. Johansson, Cfd simulations of pre-chamber jets' mixing characteristics in a heavy duty natural gas engine, JSAE/SAE 2015 International Powertrains, Fuels & Lubricants Meeting 2015-01-1890. doi:https://doi.org/10.4271/2015-01-1890.
[26] G. Kammel, F. Mair, J. Zelenka, M. Lackner, A. Wimmer, G. Kogler, E. Bärow, Simulation based predesign and experimental validation of a prechamber ignited hpdi gas combustion conceptdoi:https://doi.org/10.4271/2019-01-0259.
[27] G. Xu, Y.M. Wright, M. Schiliro, K. Boulouchos, Characterization of combustion in a gas engine ignited using a small un-scavenged pre-chamber, International Journal of Engine Research 21 (7) 1085–1106. doi: 10.1177/1468087418798918.
[28] B. Korb, K. Kuppa, H.D. Nguyen, F. Dinkelacker, G. Wachtmeister, Experimental and numerical investigations of charge motion and combustion in lean-burn natural gas engines, Combustion and Flame 212 (2020) 309–322. doi:https://doi.org/10.1016/j.combustflame.2019.11.005.
[29] A. Validi, H. Schock, F. Jaberi, Turbulent jet ignition assisted combustion in a rapid compression machine, Combustion and Flame 186 (2017) 65–82. doi:https://doi.org/10.1016/j.combustflame.2017.07.032.
[30] Malé Q, Staffelbach G, Vermorel O, Misdariis A, Ravet F, Poinsot T. Large eddy simulation of pre-chamber ignition in an internal combustion engine. Flow, Turbulence Combustion 2019;103(2):465–83. https://doi.org/10.1007/s10494-019-00026-y.
[31] Validi A, Jaberi F. Numerical study of turbulent jet ignition in a lean premixed configuration. Flow, Turbulence Combustion 2018;100(1):197–224. https://doi.org/10.1007/s10494-017-9837-7.
[32] F. Qin, A. Shah, Z.-w. Huang, L.-n. Peng, P. Tunestal, X.-S. Bai, Detailed numerical simulation of transient mixing and combustion of premixed methane/air mixtures in a pre-chamber/main-chamber system relevant to internal combustion engines, Combustion and Flame 188 (2018) 357–366. doi:https://doi.org/10.1016/j.combustflame.2017.10.006.
[33] S. Benekos, C.E. Frouzakis, G.K. Giannakopoulos, M. Bolla, Y.M. Wright, K. Boulouchos, Prechamber ignition: An exploratory 2-d dns study of the effects of initial temperature and main chamber composition, Combustion and Flame 215 (2020) 10–27. doi:https://doi.org/10.1016/j.combustflame.2020.01.014.
[34] K. Bardis, P. Kyrtatos, G. Xu, C. Barro, Y.M. Wright, K. Boulouchos, Development and validation of a novel quasi-dimensional combustion model for un-scavenged prechamber gas engines with numerical simulations and engine experiments, International Journal of Engine Research 0 (0) (0) 1468087420951338. doi:10.1177/1468087420951338.
[35] M.P.B. Musculus, K. Kattke, Entrainment waves in diesel jets, SAE International Journal of Engines 2 (11) 1170–1193. doi:10.4271/2009-01-1355.
[36] L.M. Pickett, J. Manin, C.L. Genzale, D.L. Siebers, M.P.B. Musculus, C.A. Idicheria, Relationship Between Diesel Fuel Spray Vapor Penetration/Dispersion and Local Fuel Mixture Fraction, SAE International Journal of Engines (1) 764–799. doi:10.4271/2011-01-0686.
[37] Pastor JV, López JJ, García JM, Pastor JM. A 1d model for the description of mixing-controlled inert diesel sprays. Fuel 2008;87(13):2871–85. https://doi.org/10.1016/j.fuel.2008.04.017.
[38] Abramovich GN. The theory of turbulent jets. The MIT Press Classics 1963.
[39] Bardis K, Kyrtatos P, Xu G, Barro C, Wright YM, Boulouchos K. Development and validation of a novel quasi-dimensional combustion model for un-scavenged prechamber gas engines with numerical simulations and engine experiments. Int. J. Engine Res. 2020;1468087420951338.
[40] J. Benajes, R. Novella, J. Gomez-Soriano, I. Barbery, C. Libert, Advantages of hydrogen addition in a passive pre-chamber ignited si engine for passenger car applications, International Journal of Energy Research.
[41] J. O'Connor, M.P.B. Musculus, Effects of exhaust gas recirculation and load on soot in a heavy-duty optical diesel engine with close-coupled post injections for high-efficiency combustion phasing, International Journal of Engine Research (4) 421–443. doi:10.1177/1468087413488767.
[42] Heywood JB, et al. Internal combustion engine fundamentals. McGraw-Hill New York; 1988.
[43] Novella R, Gomez-Soriano J, Martinez-Hernandiz P, Libert C, Rampanarivo F. Improving the performance of the passive pre-chamber ignition concept for spark-ignition engines fueled with natural gas. Fuel 2021;290:119971. https://doi.org/10.1016/j.fuel.2020.119971.
[44] J. Desantes, J. Pastor, J. García-Oliver, J. Pastor, A 1d model for the description of mixing-controlled reacting diesel sprays, Combustion and Flame 156 (1) (2009) 234 – 249. doi:https://doi.org/10.1016/j.combustflame.2008.10.008.
[45] Desantes J, García-Oliver J, Xuan T, Vera-Tudela W. A study on tip penetration velocity and radial expansion of reacting diesel sprays with different fuels. Fuel 2017;207:323–35. https://doi.org/10.1016/j.fuel.2017.06.108.
[46] J.V. Pastor, J.M. Garcia-Oliver, J.M. Pastor, W. Vera-Tudela, One-dimensional diesel spray modeling of multicomponent fuels, Atomization and Sprays 25 (6). doi:10.1615/AtomizSpr.2014010370.
[47] Desantes J, Payri R, Salvador F, Gil A. Development and validation of a theoretical model for diesel spray penetration. Fuel 2006;85:910–7. https://doi.org/10.1016/j.fuel.2005.10.023.
[48] Pal P, Kolodziej C, Choi S, Som S, Broatch A, Gomez-Soriano J, Wu Y, Lu T, See YC. Development of a virtual cfr engine model for knocking combustion analysis. SAE Int J Eng 2018;11(6):1069–82. https://doi.org/10.4271/2018-01-0187.